

Supplementary Information for:

Three dimensional spatiotemporal nano-scale position retrieval of diffusing nano-objects inside optofluidic microstructured fibers

Shiqi Jiang¹, Jiangbo Zhao¹, Ronny Förster¹, Stefan Weidlich¹, Malte Plidschun¹, Jens Kobelke¹, Ron Fatobene Ando¹ and Markus A. Schmidt^{1,2,3,*}

¹Leibniz Institute of Photonic Technology, Albert-Einstein-Str. 9, 07745 Jena, Germany

²Otto Schott Institute of Materials Research (OSIM), Friedrich Schiller University Jena, Fraunhoferstr. 6, 07743 Jena, Germany

³Abbe Center of Photonics and Faculty of Physics, Friedrich-Schiller-University Jena, Max-Wien-Platz 1, 07743 Jena, Germany

1. Filling of water into capillary

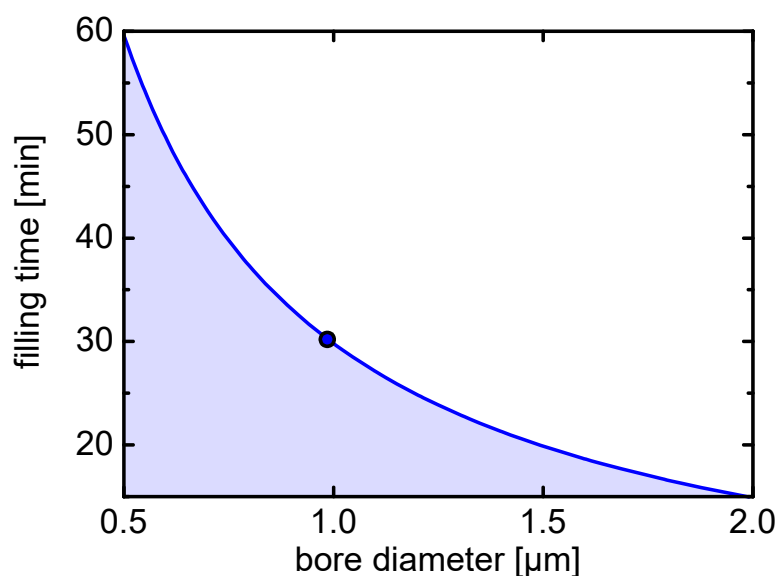


Fig. S11: Duration to fill a 5 cm long bore (in silica) with water as function of bore diameter via capillary action. The blue dot indicates the diameter of the microchannel used in the presented work.

The dynamics of filling water into the microchannel of the fiber discussed in this work are governed by the Lucas-Washburn equation [1], as due to slow filling speeds laminar flow can be assumed in all situations (Reynolds number $\ll 2300$). Neglecting external pressure allows correlating the length of the filled column l to the filling time t and the bore diameter d in the following way

$$t = \frac{4l^2\eta}{\cos(\theta)\gamma d} \quad (\text{Eq. 2})$$

with the viscosity of water $\eta = 1.003 \cdot 10^{-3} \frac{kg}{ms}$, the contact angle $\theta = 39^\circ$ (at 20°C) and the surface tension $\gamma = 0.07215 \frac{N}{m}$ [2]. Figure SI1 shows that a 1 μm bore can be filled up to a length of 5 cm at a reasonable filling time of the order of tens of minutes.

2. Diffusion of object in bulk medium

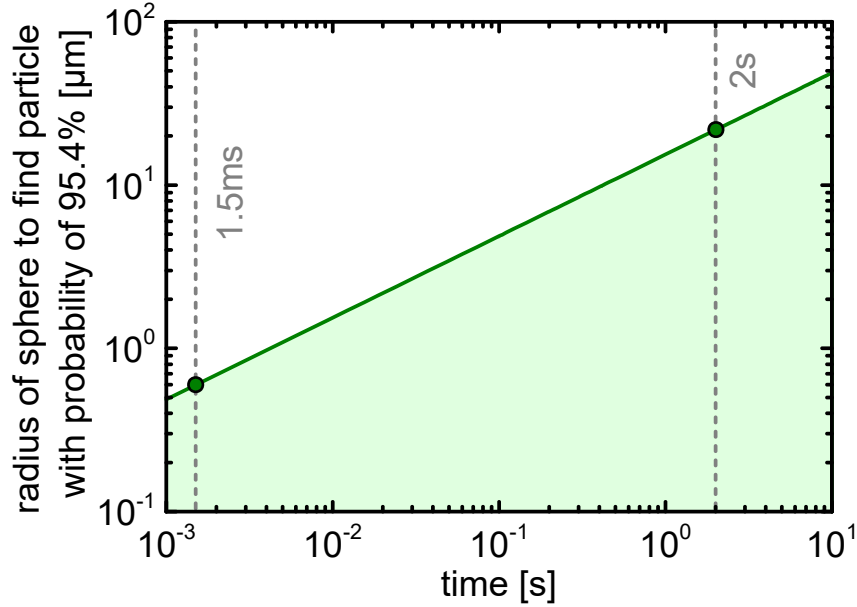


Fig. SI2: Radius of sphere to find a freely diffusing nano-particle in water with a probability of 95.45%. The left dot corresponds to track length shown in Fig. 4b, the right shows the radius for a time of 2 ms.

The discussion of the diffusion length of a particle located in a bulk medium demands to calculate the radius of the sphere the nano-object is located in with a probability of 95.45%. This sphere is given by the twice of standard deviation of the diffusion process:

$$2\sigma = 2 \sqrt{\frac{k_B T}{a\eta\pi} t_o} \quad \text{Eq. 2}$$

with the Boltzmann constant k_B , the temperature T , the nano-object radius a , the viscosity of the liquid η and the observation time t_o . In the current case (assuming water) $T = 300$ K, $a = 25$ nm and $t = 4$ s, leading to $\sigma = 15\mu m$ (Fig. SI2).

3. Nanoparticle properties

The nanoparticle ensemble we use in this work is composed of ultra-uniform gold nanospheres (nanoComposix, AUXU50) which owns a very narrow size distribution (CV < 3.4 %). The particles are dissolved in aqueous 2 mM sodium citrate with the particle concentration of 4.7×10^{10} particles/mL. The particles include a modified surface of PEG12-carboxylic acid.

The extinction cross section of gold nanoparticle in the mixture of DMSO and citrate water has been measured by a spectrophotometer (Jasco V-660) from 400 to 800 nm with a resolution of 0.1 nm, showing a clear surface plasmon resonance peak dip at around 513 nm (Fig. SI3).

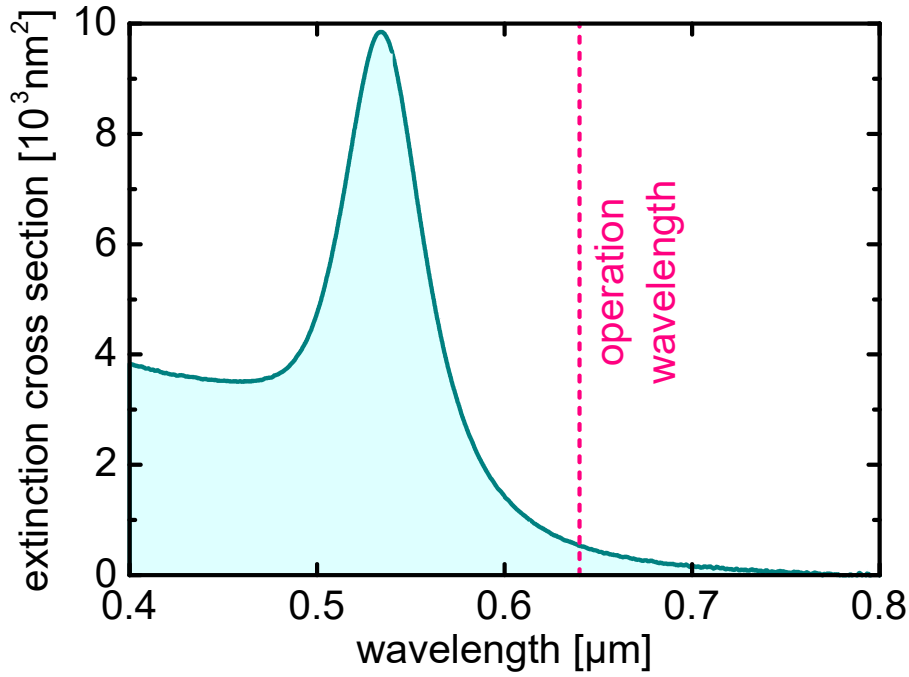


Fig. S13: Measured spectral distribution of the extinction cross section of the 50 nm gold nanoparticle ensemble used in the present work (the plasmonic peak is located in 533 nm). The vertical pink dashed line indicates the wavelength of operation (640 nm).

4. Properties of the core section and the core mode

The refractive index profile of the core follows $n(r) = (n_{max} - n_{SiO_2}) \cdot (r/a_c)^2$, where r is the radial coordinate and a_c is the core radius which is about $0.9\mu\text{m}$ for the MGIF discussed here. Given the mole fraction of GeO_2 in the center of the core is 0.235, $n_{max} = 1.4923$ and $n_{SiO_2} = 1.4568$ (dependence of refractive index on GeO_2 -content is discussed in [3]) for $\lambda = 640$ nm. The dispersions of the first four higher-order modes of the MGIF structure in absence of the microchannel are shown in Fig. S14, revealing that the fiber is single-mode at the operation wavelength as confirmed by modal analysis (inset of Fig. S14).

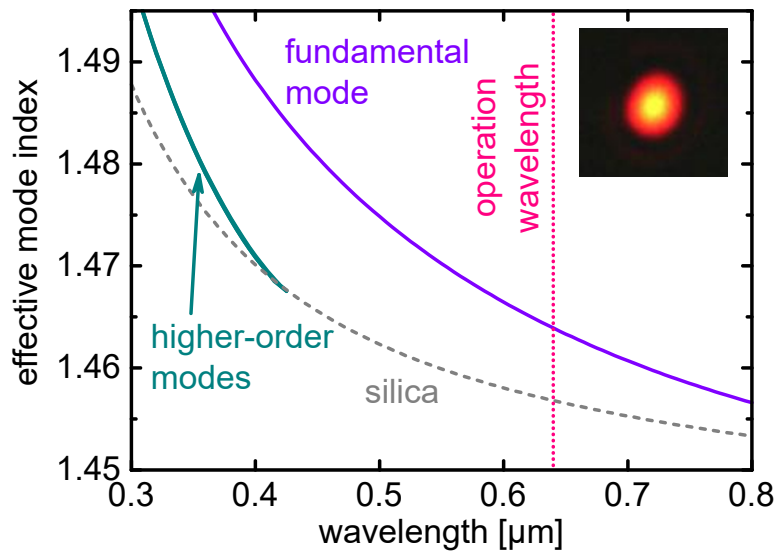


Fig. S14: Spectral distribution of the dispersion of the first four higher-order modes of the MGIF considered here in absence of the microchannel (violet: fundamental core mode, dark cyan: higher-order modes, dashed grey line: refractive index of silica). The vertical

dotted pink line indicates the wavelength of operation (640 nm). The image shows the core mode transmitted through a 50 cm long empty MGIF sample in case white light is coupled into the fiber, showing no evidence of any higher-order mode excitation.

5. Localization accuracy

The theoretical localization accuracy is given by [4]

$$\sigma = \frac{\lambda_{em}}{2\pi \cdot NA \cdot \sqrt{N_p}} = \frac{\lambda_{em}}{2\pi \cdot NA \cdot \sqrt{g \cdot I}},$$

with emission wavelength ($\lambda_{em} = 640\text{nm}$), numerical aperture ($NA = 1.25$) and the number of detected photons (N_p). The number of photons is obtained by the product of camera gain ($g = 8.4 e^-/ADU$) and intensity (counts) of a particle in one image. The brightest object has 20.000 counts, leading to a maximum theoretical localization accuracy σ_{max} of 0.4nm.

The average localization accuracy $\bar{\sigma}$ of N frames is obtained by averaging the theoretical localization accuracies σ_n of every frame:

$$\bar{\sigma} = \sum_n \frac{\sigma_n}{N} = \frac{\lambda_{em}}{2\pi \cdot NA \cdot N} \cdot \sum_n \frac{1}{\sqrt{N_p}}$$

6. Determination of localization parameters

The illuminating evanescent field in the microchannel is described by an exponential type $I(y) = I_0 \exp\left(\frac{y}{\delta}\right) + c = \exp\left(\frac{y-y_0}{\delta}\right) + c$ as is shown in Figs. 1(e) and (f). The characteristic parameters - decay parameter δ and offset c - need to be determined from the measurement data, as simulations might not entirely describe the actual experimental situation. Here we use an approach that relies on calculating the intensity histogram of the tracked particle and fit the theoretical expectations to it, as explained in the following.

The histogram has equidistant intensity bins of width ΔI . Each bin shows the number of frames the particle has the intensity of that bin. The probability P of the scattered intensity of a particle to be in a specific intensity bin is given by the product of the spatial area this intensity occurs in the microchannel Δy and the probability of a particle to be in this area p.

With the known shape of the evanescent field, each intensity bin ΔI corresponds to a well-defined spatial bin in the microchannel $\Delta y(I, \Delta I)$ at the location of this particular intensity:

$$\frac{\Delta I}{\Delta y} \approx \frac{dI}{dy} = \frac{I_0 \exp(y/\delta)}{\delta} = \frac{I(y) - c}{\delta}$$

$$\Delta y(I, \Delta I) = \frac{\delta}{I(y) - c} \cdot \Delta I$$

It can be seen, that due to the non-linear shape of the evanescent field, the spatial bins $\Delta y(I, \Delta I)$ are not equidistant. As a result high intensities are found in small areas, while low intensities are spread over larger areas (compare Fig. S15).

The probability $p(y)$ of a particle to be at a specific spatial position y is not a constant either due to the circular shape of the microchannel. It is proportional to the chord of the microchannel along the x -coordinate as it is visualized in Fig. S15:

$$p(x) \sim 2 \cdot x = 2 \cdot \sqrt{r^2 - y^2} = p(r, y)$$

Finally, the probability P of scattered intensity of a particle to be in a defined intensity bin is given by (compare green area in the microchannel in Fig. S15, bottom):

$$P \sim \Delta y(I, \Delta I) \cdot p(r, y) = \frac{\delta}{I(y) - c} \cdot \Delta I \cdot 2 \cdot \sqrt{r^2 - y^2}$$

Replacing the spatial coordinate y by the shape of the evanescent field $I(y)$ leads to:

$$P \sim \frac{2\delta \cdot \Delta I}{I - c} \cdot \sqrt{r^2 - \delta \cdot \ln \left[\frac{I - c}{I_0} \right]^2}$$

Since the integral of the probability P must be normalized to 1, the size of the intensity bin ΔI can be disregarded. The radius r is replaced by the known diameter d_y of the microchannel that has been determined by the study related to Fig. 2 (c):

$$P(I, \delta, c, I_0) \sim \frac{\sqrt{\left[\frac{d_y}{2} \right]^2 - \delta \cdot \ln \left[\frac{I - c}{I_0} \right]^2}}{I - c}$$

This function $P(I, \delta, c, I_0)$ is fitted to the corresponding experimental data – the intensity histogram of the data – to obtain the evanescent field parameters δ and c . The amplitude I_0 is irrelevant, because it is only a shift y_0 of the coordinate system. The fit uses again a penalty function to avoid local minima and complex-valued probabilities due to the square root term.

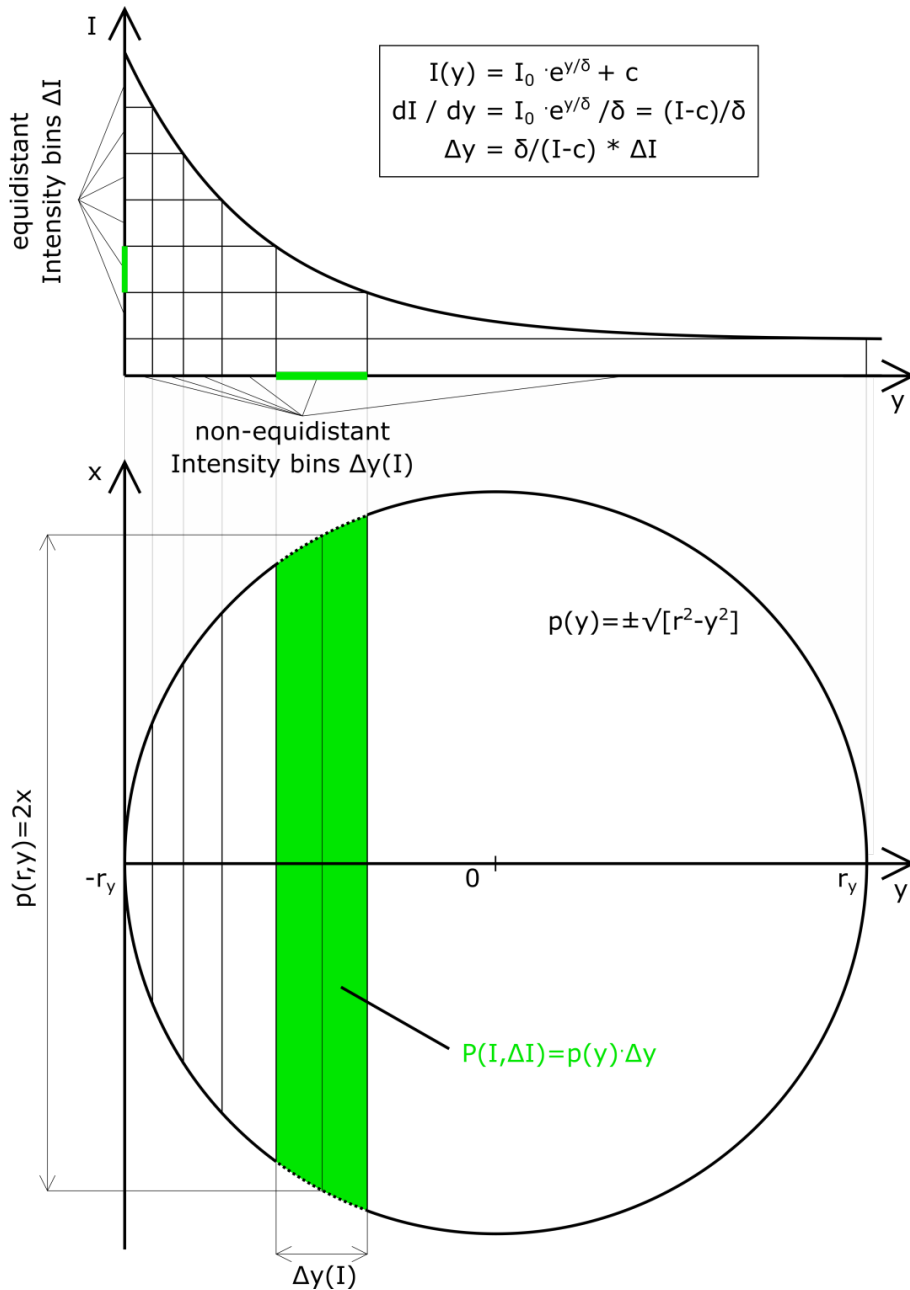


Fig. S15: Top: Spatial distribution of the evanescent field $I(y)$, correlating the intensity bins ΔI (green line on I axis) to the spatial bin Δy (green line on y -axis). Bottom: the shape of the microchannel defines the probability p of a particle to occur in a specific spatial bin. Thus, the probability of a particle to scatter with a specific intensity regime $P(I, \Delta I)$ is $\Delta y \cdot p$ which represents the green area in the microchannel.

7. Fiber-based nanoparticle tracking within the context of total internal reflection

For a classification of the fiber-approach within the context of existing technology for 3D tracking it is important to compare the presented concept to schemes that involve evanescent fields. Here it is important to consider that the formation of modes and thus evanescent fields inside optical fibers can in fact be explained in a first order approximation by a ray-type model that describe optical modes by the interference of two oppositely zigzagging beams that reflect at the core/cladding boundary. This model naturally suggests a clear correlation between total internal reflection

illumination (as for instance in total internal reflection microscopy (*TIRM*)) and illumination via optical modes: *TIRM* involves one single reflection and thus the extend of the evanescent field is limited to the size of the incoming beam, while the interference of the two zigzagging beams in the waveguide case leads to a homogenous (translational invariant) illumination along the entire fiber. Note that the fiber-related scheme can be regarded as “ideal” light-line illumination, as in contrast to Gaussian beam illumination the fiber approach does not show diffraction, i.e., the object experiences the same intensity distribution at any longitudinal position inside the waveguide.

In the following one particular benefits of the fiber approach (referred as *MGIF*-approach) in relation to total internal reflection is discussed in more detail.

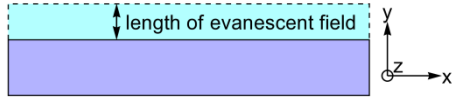
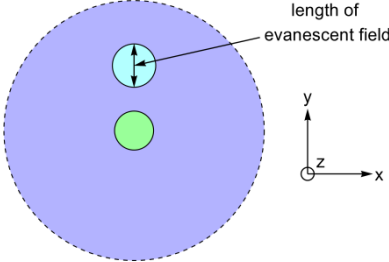
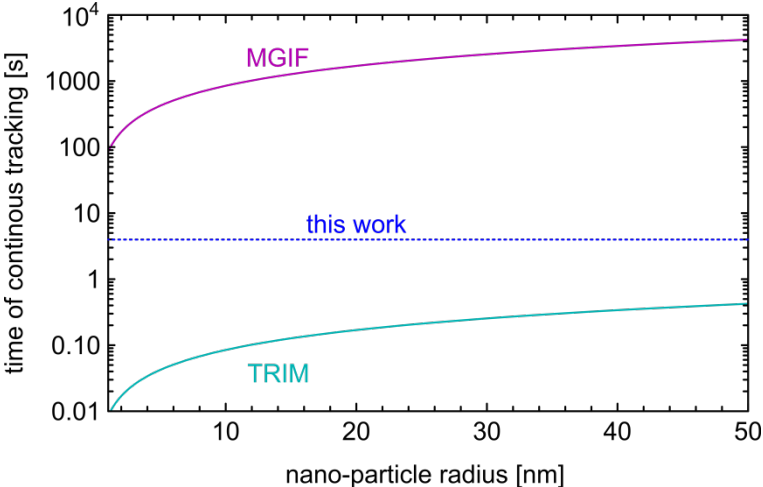
Confinement of the particles to a microchannel: The fiber channel provides an intrinsic micro-scale confinement to the diffusing nano-objects. This confinement is particular important for the tracking of fast moving objects, since the Brownian motion of the objects generally imposes them to leave the area of observation after a certain time, making the tracking of in particular nano-scale objects over long time scales challenging. In the following the advantages of the fiber geometry with regard to this aspect is presented by a comparing the diffusion properties and the achievable accuracy in measuring particle diameters:

A. Estimation of time of continuous nano-object observation

In order to observe single events and for obtaining significant particle statistics, it is highly desirable to observe the diffusion of the nano-object of interest for an as-long-as-possible duration. In this context the following section compares the *TIRM*- and the *MGIF*-approaches in terms of longest theoretically possible time to continuously track a single particle via analyzing the diffusion of a nano-particle of radius $a = 25\text{nm}$, which is correlated to the diffusion coefficient D via $D = k_B T / 6a\pi\eta$ (viscosity of water $\eta = 3.7 \cdot 10^{-3}\text{Pa} \cdot \text{s}$ at the temperature $T = 273\text{K} + 25\text{K}$). This time t_i^{con} can be defined by the correlation between the mean-square-displacement along one principal axis (coordinate defined as q_i with $i = x, y, z$) and the time, yielding $t_i^{\text{con}} = \langle q_i^2 \rangle / 2D = L_i^2 / 2D$ with the distance L_i along which the object can be detected [5]. Since this equation relates to the variance of the Gaussian distribution of the diffusion of the nano-object, t_i^{con} yields a probability of 68% that the particle is located inside the spatial interval $0 \leq q_i \leq L$. Therefore it can be assumed that for times $t > t_i^{\text{con}}$ the nano-object has left the region of detection and cannot be tracked anymore, allowing for defining the time for continuously tracking the nano-object by $t^{\text{con}} = \min(t_x^{\text{con}}, t_y^{\text{con}}, t_z^{\text{con}})$. Both *TIRM* and *MGIF* rely on evanescent field sensing and due to the mentioned similarity between mode formation and total-internal reflection the spatial extensions of the respective evanescent field are assumed to be $1\mu\text{m}$ for both cases (for details see Tab. S11), while in the *MGIF* case this corresponds to the diameter of the microchannel.

For unconfined *TIRM* (left column in Tab. S11), the nano-object is lost once it leaves the evanescent field along the y -direction ($L_y = 1\mu\text{m}$), yielding $t^{\text{con}} = 0.211\text{s}$ while within the xz -plane $t_{x,z}^{\text{con}}$ is defined by the spatial extension of the illumination beam, which is assumed to be $L_x = 100\mu\text{m}$ and $L_z = 100\mu\text{m}$. In case of the *MGIF*-approach (left column in Tab. S11), in contrast, the extension of the evanescent field is identical to the diameter of the channel, and thus the lateral confinement provides continuous particle tracking across the xy -plane, while the object can only leave the region of observation by diffusing along the z -direction. Assuming an identical field of view ($L_z = 100\mu\text{m}$) yields $t_{\text{MGIF}}^{\text{con}} = 35\text{min}$, which is about 10^4 longer than in unconfined *TIRM*, clearly demonstrating

the benefits of the MGIF-approach. Note that in the experiments presented in this work the maximum time of continuous tracking has not been reached due to the camera settings used in the experiments. Here the object has been tracked for maximal $t_{track} = 4s$ (horizontal dashed line in the bottom plot in Tab. SI1), which is already significantly above to what can be achieved by *TIRM*. It is important to note that we recently found out that modified camera settings and improved computer hardware allows for acquiring substantially longer tracks. Principally, the current system should allow for recording tracks with a maximal number of frames of $12 \cdot 10^6$ at frame rates of 2kHz, translating into a track length of at max 1.5 hours. Therefore we anticipate conducting a series of new experiments for the observation of nano-object diffusion over a time scale of several tens of minutes.

	Total Internal Reflection Microscopy (TIRM)	Modified Step Index Fiber (MGIF)
geometry		
(L_x, L_y, L_z)	(100 μ m, 1 μ m, 100 μ m)	($\infty, \infty, 100\mu$ m)
$(t_x^{con}, t_y^{con}, t_z^{con})$	(35min, 0.211s, 35min)	($\infty, \infty, 35$ min)
t^{con}	0.211s	35min
dependence on particular diameter		

Tab. SI1: Comparison of the time of continuous tracking in case of *TIRM* (left) and *MGIF* (right). The top row represents the respective geometry including the relevant parameters. The parameters of the second and third rows have been defined in the text. The plot in the bottom row shows a comparison of continuous tracking time as a function of particle diameter for the *TIRM* (cyan) and the *MGIF* (magenta) approaches. The horizontal dashed line refers to the time of continuous tracking used in this work.

B. Precision of diameter determination

A consequence of this improvement in continuous observation time is the larger number of frames per trajectory significantly improving the statistics regarding determination of particle diameters. This improvement is visible via the Cramér–Rao lower bound (CRLB), showing that the standard

deviation of the diffusion coefficient σ_D is correlated to the total number of frame N via $\sigma_D \sim 1/\sqrt{N}$. For instance, assuming $a = 25\text{nm}$ the continuous tracking times for the two methods calculated in the previous sections yield $N_{\text{TIRM}} = 4.23 \cdot 10^2$ and $N_{\text{MGIF}} = 4.23 \cdot 10^6$ (assuming a frame rate of $\nu = 2003\text{Hz}$) showing a theoretical improvement by the MGIF-approach by a factor of 10^4 . Assuming the same frame rate for *TIRM* and *MGIF*, the maximal theoretical achievable accuracy improvement $\delta\sigma$ can be calculated by the ratio of the standard deviations of *TIRM* and *MGIF* which via the the Cramér–Rao lower bound leads to $\delta\sigma = \sigma_{\text{TIRM}}/\sigma_{\text{MGIF}} = \sqrt{N_{\text{MGIF}}/N_{\text{TIRM}}} = 100$ for any particle diameter using the previously stated extension of the evanescent fields. This number clearly shows a substantial improvement of the accuracy regarding diameters determination when using the MGIF-approach. Within the experiments shown here, the maximum track length was $t_{\text{track}} = 4\text{s}$ at a frame rate of $\nu = 2\text{kHz}$, yielding $N_{\text{exp}} = 8000$. Assuming $a = 25\text{nm}$ gives $\delta\sigma = \sqrt{N_{\text{exp}}/N_{\text{TIRM}}} = 4.3$ which is significant improvement already for the system investigated here. It is particular important to note that the improvement gets substantially enhanced for smaller particle diameters (Fig. S16) and significantly increase for longer tracks.

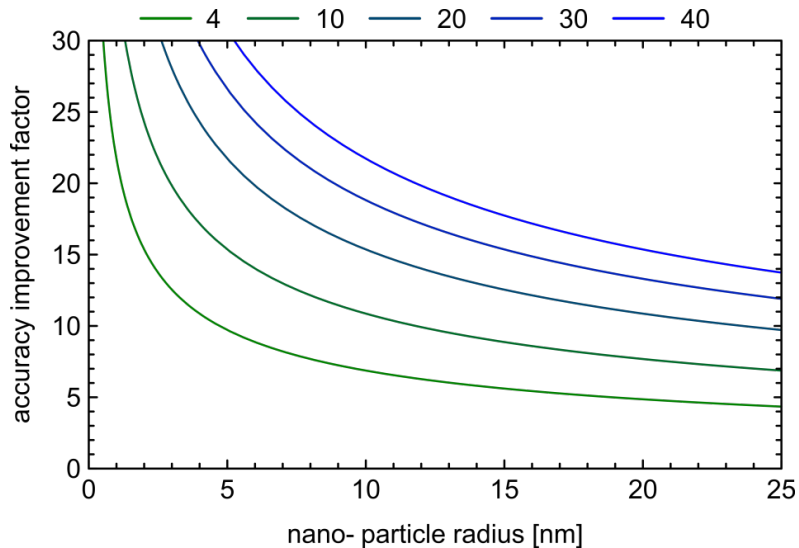


Fig. S16: Accuracy improvement factor as a function of nanoparticle radius for different track length (defined in the top legend (in units of seconds), frame rate $\nu = 2003\text{Hz}$). The case of $t_{\text{track}} = 4\text{s}$ (most green curve) corresponds to the experimental situation discussed here.

8. Visualization of different illumination geometries

To demonstrate the benefit of the fiber-mediated confinement the Brownian random walk of a single diffusing nano-object was simulated for different microscopic illumination strategies (wide-field, confocal, light sheet and light line, see supplementary information video). Moreover, we implemented the situations of two microstructured fibers, namely the antiresonant hollow core fiber (ARHCF) and the microstructured gradient index fiber (MGIF).

All illuminations include the same number of photons which are distributed with regard to the respective illumination across the specimen. The images contain Poisson noise only. Physical properties like scattering cross-section, detection efficiency or diffusion coefficient have no influence on the various types of illumination. The different illumination configurations lead to a different signal of the particle on the detector which is summarized in the table below.

The wide-field illumination (green line) spreads the illumination power over the largest area, leading to an overall low intensity and a small signal-to-noise ratio (SNR) of the particle, while the particle is always visible.

The light sheet illumination (yellow line, top view) focusses the light along one direction, leading to a higher intensity and thus a higher SNR. However the particle can leave the area of illumination along one direction (here vertical direction), so that it is dark and creates no signal (yellow line drops below wide-field signal).

The confocal configuration (magenta line) focusses the light along two dimensions leading to identical effects than the light sheet configuration, but in an even stronger way due to the smaller illumination area. In comparison to light sheet, the principal signal is higher, but drops more often below the noise floor since the particle can leave the area of illumination in two instead of just one directions. Therefore the benefit of having a large signal comes on the expense of a reduced illumination area, which allows the object to leave the smaller illumination area sooner, defining a need for a higher intensity across a larger area.

The illumination area of the confocal geometry can be enhanced by sending the light from the side and not through the detection objective, leading to a light line illumination (black line). Thus, a confocal-type illumination at high intensity is achieved in good approximation everywhere along this line. The diffraction of the beam can be in practice small, since a beam diameter of $13\mu\text{m}$ has a Rayleigh length of $200\mu\text{m}$ which is equivalent to field of view of a 63x objective. Compared to the light sheet case the same signal can be detected while the particle is lost less often. Here light sheet and light line illumination show identical behaviours while, however, the light line has higher intensity, since the photons are within the plane of focus for longer times.

The ARHCF configuration (blue line) is identical to the light line case while, however, the particle cannot leave the channel, leading to a constant high signal with no signal break-down at any time shown here.

The MGIF case (red line) is identical to the ARHCF situation, while having an overall lower power, since the object of interest probes the evanescent field of that light line configuration, which as shown in this work allows to encode the hidden axial position of the particle in its intensity. In addition, the $1.4\mu\text{m}$ diameter core of the MGIF guides the light beyond beam divergence, because such a small beam waist has a Rayleigh length of just $2.4\mu\text{m}$.

	Wide-field	Confocal	Light Sheet	Light Line	Light Line (confined, fiber)
Signal	low	high / very high	moderate	very high	very high
Particle observation Time	long	short	short	short	high

Note that at some point of time, depending on frame rate, laser intensity and diffusion coefficient, any particle will leave the illuminated area while a long observation of a small nano-object is only possible via the confinement of the fiber approaches shown here.

References

- [1]. E. W. Washburn, The dynamics of capillary flow. *Phys. Rev.*, 1921, **17**, 273-283 .
- [2]. K. Schäfer, H. H. Landolt, and R. Börnstein, *Eigenschaften der Materie in ihren Aggregatzuständen: Transportphänomene, Kinetik homogene Gasgleichgewichte* (Springer, 1968).
- [3]. J. W. Fleming, Dispersion in GeO₂-SiO₂ Glasses. *Appl. Opt.* , 1984, **23**, 4486-4493.
- [4]. Ober R. J., Ram S., and Ward E. S. Localization accuracy in single-molecule microscopy. *Biophys. J.*, 2004, **86**, 1185-1200.
- [5]. Einstein, A., Über die von der molekularkinetischen Theorie der Wärme geforderte Bewegung von in ruhenden Flüssigkeiten suspendierten Teilchen. *Ann. Phys.* , 1905, **322**, 549-560.
- [6]. Saxton, M.J., Single-particle tracking: the distribution of diffusion coefficients. *Biophys. J.*, 1997. **72**, 1744-1753.